

# Bending stiffness of biological membranes: What can be measured by neutron spin echo?\*

Michael Mell<sup>1</sup>, Lara H. Moleiro<sup>1,2</sup>, Yvonne Hertle<sup>3</sup>, Peter Fouquet<sup>4</sup>, Ralf Schweins<sup>5</sup>, Iván López-Montero<sup>1</sup>, Thomas Hellweg<sup>3,a</sup>, and Francisco Monroy<sup>1,b</sup>

<sup>1</sup> Departamento de Química Física I, Universidad Complutense de Madrid, E-28040 Madrid, Spain

<sup>2</sup> Physikalische Chemie I, Universität Bayreuth, Universitätsstraße 30, D-95447 Bayreuth, Germany

<sup>3</sup> Physikalische und Biophysikalische Chemie I, Universität Bielefeld, Universitätsstraße 25, D-33615 Bielefeld, Germany

<sup>4</sup> TOF/HR Group, Institut Laue Langevin, 6 rue Jules Horowitz, BP156, F-38042 Grenoble Cedex 9, France

<sup>5</sup> DS/LSS - ILL Soft Matter Partnership Lab, Institut Laue Langevin, 6 rue Jules Horowitz, BP156, F-38042 Grenoble Cedex 9, France

Received 9 October 2012 and Received in final form 10 April 2013

Published online: 16 July 2013 – © EDP Sciences / Società Italiana di Fisica / Springer-Verlag 2013

**Abstract.** Large vesicles obtained by the extrusion method represent adequate membrane models to probe membrane dynamics with neutron radiation. Particularly, the shape fluctuations around the spherical average topology can be recorded by neutron spin echo (NSE). In this paper we report on the applicable theories describing the scattering contributions from bending-dominated shape fluctuations in diluted vesicle dispersions, with a focus on the relative relevance of the master translational mode with respect to the internal fluctuations. Different vesicle systems, including bilayer and non-bilayer membranes, have been scrutinized. We describe the practical ranges where the exact theory of bending fluctuations is applicable to obtain the values of the bending modulus from experiments, and we discuss about the possible internal modes that could be alternatively contributing to shape fluctuations.

## 1 Introduction

The bending stiffness is one of the most relevant mechanical characteristics in the description of the stress response of biological membranes [1]. This mechanical parameter is closely related to the internal cohesion of the lipid bilayer, which is ultimately determined by structural parameters such as the bilayer thickness, the average molecular area occupied by lipids in the monolayers and the interactions involved to form the bilayer. Classical diffraction approaches have been extensively exploited to study structural parameters in lyotropic phases using X-ray methods [2]. The most popular method consists of measuring diffraction signals in samples composed of multilamellar stacks of lipid bilayers to construct electron density profiles from the intensities of the diffraction peaks and from the shapes of the distributions. Small angle scattering methods, particularly with X-rays (SAXS), have provided a successful option to determine the elastic moduli of a lyotropic array [3,4]. However, a closer look at the real thing requires methods able to probe mechanics of single lipid

bilayers. Unilamellar vesicles are attractive because they are topologically and structurally equivalent to biological membranes. Similarly to lipid bilayers in living cells, they are constituted of a continuous membrane enclosing a liquid compartment separated from a solvent exterior. Diluted dispersions of large unilamellar vesicles (LUVs) can be easily prepared with a narrow distribution of vesicle sizes, providing a statistical population for optimal ensemble averaging of the mechanical properties of a high number of identical bilayers. However, instead of having intense diffraction peaks as in highly dense multilamellar arrays, scattering from dilute dispersions of unilamellar vesicles is much weaker and diffuse, making the scattering intensities practically undetectable at high wave vectors. It is precisely at high wave vectors where small-scale mechanical deformations might be distinguished from the static form factor of the spherical vesicle. Since higher contrast is achieved with specimen hydrogen atoms in solvent deuterated samples, neutron radiation provides an excellent alternative to X-rays to assess structure in biological matter [5,6]. Moreover, cold neutrons do not cause any beam damage in the organic material. Therefore, small angle neutron scattering (SANS) was proposed to study the structure of lipid bilayers in unilamellar vesicles [7]. The most popular analysis deals with fitting SANS profiles to form-factor models accounting for the spherical shell ge-

\* Contribution to the Topical Issue “Neutron Biological Physics” edited by Giovanna Fragneto and Frank Gabel.

<sup>a</sup> e-mail: thomas.hellweg@uni-bielefeld.de

<sup>b</sup> e-mail: monroy@quim.ucm.es

ometry of the vesicle and for details of the inner bilayer structure [8–10]. However, although increasingly realistic models of membrane structure can be defined, the diffuse contribution from mechanical fluctuations is not easily accounted for being usually interpreted as a smearing component in the SANS profile due to structural polydispersity. Hence, energy-resolved scattering methods represent the optimal choice for directly detecting shape fluctuations of vesicle membranes. The stochastic signal due to shape fluctuations can be rationalized as a correlated contribution to the scattering from all the different scatters in the vesicle. In particular, neutron spin echo (NSE) provides the adequate  $q$ -range to quantitatively probe fast fluctuation dynamics over small lengths typical for these nanometer-sized vesicles. Therefore, an approach based on NSE experiments performed on diluted LUV dispersions is advantageous for studying membrane mechanics. First and foremost, NSE probes the dynamics of isolated single bilayers. As an added convenience, diluted samples can be used which minimizes the interaction between the membranes and reduces mutual perturbation. Moreover, the technique is non-invasive. In addition, NSE provides an ensemble average over a large population of vesicles, a determinant advantage over single-vesicle methods. Additionally, sufficient neutron contrast is endowed with only solvent deuteration (use of heavy water), which makes lipid vesicle membranes “visible” in a neutron-transparent medium. Using LUVs in the 100 nanometer size domain, NSE might be adequate for studying the relaxation dynamics of the shape undulations in the regime of high scattering wave vectors compared to vesicle dimensions, *i.e.*  $qR \gg 1$  ( $q$  is the modulus of the 3D scattering vector and  $R$  the vesicle radius). In the NSE dynamic window, shape fluctuations appear coupled together with translational effects, which can be conveniently unfolded by complementary measurements of the vesicle radius using dynamic light scattering (DLS) [11, 12]. The aim of the present contribution is to shed light on the problem of vesicle dynamics in the context of the analysis of dynamic scattering data. To our best knowledge only a very limited number of works directly investigate the thermally excited undulations of unilamellar lipid vesicles. In the present article, we report on NSE measurements of vesicle fluctuations performed on two different classes of membrane systems, lipid bilayers and polymer membranes. Ideally thin, sheet-like, membranes undergo shape fluctuations exclusively governed by bending elasticity. Lipid membranes, however, self-assemble as a tail-to-tail bilayer, a structural detail which could introduce additional contributions to its fluctuation dynamics. Particularly, curvature fluctuations coupling transverse bending with longitudinal compression could be relevant at high wave vectors [13], where local curvature causes a strong distortion of the lipid distribution in each monolayer leaflet. Conversely, if a compact sheet-like structure was considered, as with copolymer membranes, pure transversal bending deformations can be considered to exist separately from longitudinal motions. In this case, a simple theory of bending elasticity might be sufficient to account for the shape fluctuations of vesicle membranes. In bilayers, however, curvature mo-

tions are largely influenced by dilatational stresses whose dynamics is governed by the relative sliding between the two monolayers [13]. Such a hybrid mode of curvature motion could eventually contaminate the pure-bending response making an extension of the theory to compression elasticity necessary. In the next section, we describe the minimal theory necessary to rationalize the pure-bending shape fluctuations in terms of the bending stiffness of the membrane, with an emphasis on their applicability limits beyond which, another classes of curvature motion could eventually come into play.

## 2 Theory

The dynamics of the curvature undulations of elastic membranes is usually described by the Helfrich-Canham Hamiltonian for the bending deformation [1] in combination with linear hydrodynamics in the viscous regime [14, 15]. If inertial terms are neglected, the hydrodynamic equations can be resolved in the Stokes-limit and thus dynamic correlations arise from the balance between elastically restored motion (driven by the bending stiffness,  $\kappa$ ) and viscous dissipation (governed by the bulk viscosity,  $\eta$ ) [15]. When the linear dynamical equations are resolved for the bending fluctuations described as 2D planar waves in a flat membrane ( $k = |\mathbf{k}|$  is the modulus of the in-plane wave vector of the transversal fluctuation), the height-to-height autocorrelation function is obtained as [14–16]

$$\langle h_{\mathbf{k}}(t)h_{-\mathbf{k}}(0) \rangle = \langle h_{\mathbf{k}}^2 \rangle_B e^{-\omega_B(k)t}, \quad (1)$$

with the amplitude given as the ratio between the thermal energy and the elastic energy of the bending mode, as predicted by the equipartition theorem [16, 17]

$$\langle h_{\mathbf{k}}^2 \rangle_B = \frac{k_B T}{\kappa} \frac{1}{k^4}. \quad (2)$$

Notice that weaker fluctuations correspond to stiffer membranes. The time dependence of the bending modes is governed by a  $k^3$ -dependent relaxation rate

$$\omega_B(k) = \frac{\kappa}{4\eta} k^3, \quad (3)$$

which becomes faster with increasing bending stiffness.

The above treatment considers the membrane translationally immobile, where only the bending fluctuations are accounted for. In a more complete theory for vesicles, they are assumed to perform translational motions by diffusion in the medium as a whole. Bending modes appear as a series of internal modes accounting for the shape fluctuations. In the case of spherical membranes, *e.g.* vesicles or emulsion droplets, the corresponding intermediate scattering function might be written as a function of the 3D scattering vector as [18, 19]

$$S(q, t) = e^{-\Gamma_T t} [A_T(q) + A_B(q)S_B(q, t)], \quad (4)$$

with  $\Gamma_T$  being the diffusive rate of the translational motion

$$\Gamma_T = D_T q^2, \quad (5)$$

where  $D_T$  is a translational diffusion coefficient given by the Stokes-Einstein formula

$$D_T = \frac{k_B T}{6\pi\eta R}. \quad (6)$$

On the one hand,  $A_T(q)$  accounts for the relative amplitude of the translational mode, which is proportional to the size of the diffusing object. On the other hand,  $A_B(q)$  accounts for the relative contributions of the internal modes, *i.e.* the shape fluctuations whose effective time dependence is given by the dynamic function  $S_B(q, t)$ . The two relative amplitudes should be defined in a way such that they are mutually normalized [18], *i.e.*  $A_T + A_B = 1$ . Within the hydrodynamic theory, Milner and Safran (MS) described the fluctuation dynamics of spherical membranes, *e.g.* microemulsion droplets and vesicles [20]. The MS theory couples dynamically the normal bending modes of the flexible spherical membrane with the effective viscous friction exerted by the bulk solvent [20]. In that case, the hydrodynamic equations are solved for the surface modes described as spherical harmonics, which constitute the natural ansatz for the shape fluctuations in the spherical topology. For membranes with a zero spontaneous curvature, at thermal equilibrium, MS describe bending fluctuations as normal modes defined by the spherical harmonics characterised by the integer number  $l$  which determine the discrete values of the fluctuation wave vector,  $k(l) = l/R$  ( $l = 2, 3, 4, \dots, \infty$ ). The time dependence is overdamped, characterized by an autocorrelation function as in eq. (1) [20]. For spherical tensionless vesicles, the relaxation rate of the discrete modes is  $\omega_B = (\kappa/\eta R^3)l(l+1)/Z(l)$ , with  $Z(l) = (2l+1)(2l^2+2l-1)/l(l+1)(l+2)(l-1)$ . At high  $k$ , such discrete modes converge to the continuous solution of the planar membrane; if  $kR (= l) \gg 1$ , the dimensionless geometric factor takes the approximate value  $Z(l) \approx 4/l$ , thus  $\omega_B \approx (\kappa/4\eta)k^3$ , the dispersion law of the bending modes in the planar membrane (see eq. (3)). In the MS theory, the translational contribution to scattering is essentially determined by the static structure factor of the diffusing object,  $A_T(q) = 4\pi[j_0(qR)]^2$ ,  $j_0$  being the zeroth-order spherical Bessel function [20]. With respect to the contribution due to shape fluctuations, all the discrete bending modes ( $l \geq 2$ ) contribute to their structure factor proportionally to the spectral amplitudes weighted by a modulation factor [20]

$$A_B(q)S_B(q, t) = \sum_{l \geq 2} F_l(qR) \langle h_l^2 \rangle_B e^{-\omega_B(l)t}, \quad (7)$$

where the weighting factor  $F_l$  is given by

$$F_l(z) = (2l+1) [(l+2)j_l(z) - zj_{l+1}(z)]^2, \quad (8)$$

with  $j_l(qR)$  standing for the  $l$ -th order spherical Bessel function.

For the spherical geometry, eq. (7) describes the dynamic structure factor of the shape fluctuations as a discrete sum of exponential decays accounting for the relaxation of all the spherical modes projected on the observed

scattering direction. In the case of a dynamics dominated by bending modes, *i.e.*  $\langle h_k^2 \rangle \sim k^{-4}$ ,  $\omega_k \sim k^3$ , an effective stretched-like relaxation might arise from the sum of modes in eq. (7). In rigid membranes ( $\kappa \gg k_B T$ ), the amplitudes of the bending modes are extremely weak thus being quite inefficient in exploring volume. Furthermore, they are strongly damped thus the effective dissipation becomes partially frustrated. Consequently, only the complete description in eq. (7) provides adequate account of the collective fluctuation dynamics. However, in the particular case of floppy membranes undergoing large shape fluctuations, a given spherical mode of fluctuation dominates at the narrow spatial scale determined by the observed wave vector. In these cases ( $\kappa \approx 0$ ), we mainly observe scattering from a single-fluctuation mode,  $k_{\text{dom}} \approx q$  ( $= l_{\text{dom}}/R$ ); then, the multimodal description in eqs. (7)-(8) can be in practice reduced to a single-mode approximation [21]

$$S_B^{(0)}(q, t) \approx \exp(-\Gamma_{\text{MS}} t), \quad (9)$$

with a relaxation rate corresponding to the decay rate of the congruent bending mode, this is  $\Gamma_{\text{MS}} \approx \omega_B = (\kappa/4\eta)q^3$  (see eq. (3)).

For vesicle phases, such a single-exponential approach is only a crude approximation. Exception is the case of parallel scattering from an oriented lamellar phase, where the relaxation rate of the dynamic structure factor coincides with the mode relaxation rate [22, 23]. With respect to the fluctuation amplitudes, we plot in fig. 1A the prediction of the MS theory for the normalized amplitude of the translational mode of the spherical vesicle as a function of the reduced wave vector. For monodisperse spheres, the amplitudes display an oscillatory pattern, with a decreasing envelope indicating the progressive decrease of the translation amplitude in favor of the bending fluctuations. When size polydispersity is considered, the scattering amplitudes should be averaged over the equilibrium distribution of vesicle sizes. In those cases, increasing polydispersity causes the oscillations to progressively smear out, finally disappearing into a monotonic pattern clearly indicating the progressive influence of the bending fluctuations on the dynamic structure factor (see fig. 1A). Because high bending stiffness causes a dramatic decrease of the shape fluctuations (see eq. (2)), the MS theory predicts a progressively decrease of the amplitude of the bending contribution ( $A_B$ ) with respect to the bare translational mode ( $A_T \gg A_B$ ). This effect is shown in fig. 1B, where a  $\kappa$ -dependent crossover between a translation-dominated regime at low  $q$ 's and a fluctuation-dominated regime at high  $q$ 's can be observed.

The MS theory has been productively exploited in the dynamical description of the shape fluctuations of floppy droplets in microemulsion phases ( $\kappa \approx 0$ ) detected by NSE [21, 22, 24–29]. However, it has rarely been applied to scrutinize lipid vesicle systems [11, 12, 30]. When applied to rigid membranes ( $\kappa \gg 0$ ), the single-mode MS approach (eq. (9)) only leads to a qualitative interpretation of the  $q^3$ -dependences of the relaxation rates. However, it fails to give realistic values for the elastic constant,  $\kappa$ . For lipid bilayers,  $\kappa$  should be of the order of

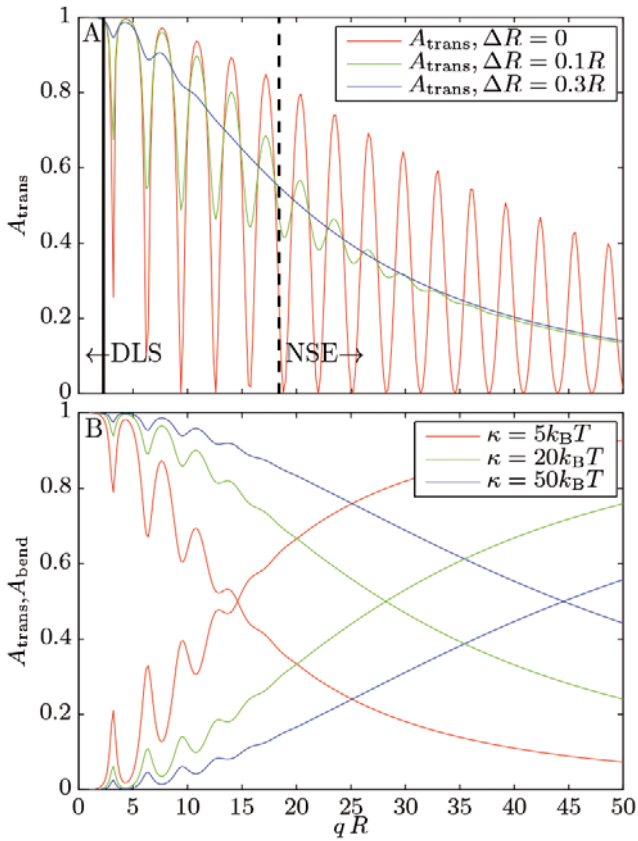


**Fig. 1.** A) Amplitudes of the translational component according to theory by Milner and Safran. The three plots show three different cases of polydispersity  $\Delta R$  for a membrane of bending rigidity  $\kappa = 10k_B T$ . The effect of the polydispersity enters as a convolution and was computed numerically. The vertical lines delimit the wave vector range accessible to DLS and NSE for  $R = 100$  nm vesicles. B) Amplitudes of translation and bending modes for three different bending rigidities at a polydispersity of  $\Delta R = 0.2R$ .

5–20 in  $k_B T$  units, however, significantly higher values are obtained when the NSE relaxation rates are discussed in view of the classical MS theory. Furthermore, early experiments with lipid lamellar phases and vesicle suspensions already demonstrated large deviations of the NSE relaxation profiles from the single-exponential behavior of eq. (9) [22, 31, 32]. Although being analytically exact, the complete MS scheme based on discrete spherical harmonics modes is quite difficult to implement in fitting algorithms. Furthermore, collective averaging in polydisperse samples prevents the detailed detection of the oscillatory features linked to the spherical structure factor. Moreover, NSE probes shape fluctuations at high  $q$ 's determined by the observational set-up, which do not necessarily coincide with the discrete wave vectors of the spherical harmonics ( $k = l/R$ , with  $l \geq 2$ ). Therefore, for large lipid vesicles probed by NSE at high wave vectors ( $qR \geq 5$ ), instead of the discrete spherical harmonics, a continuous approximate solution as planar waves is possible to describe the bending fluctuations [33, 34]. In these cases, the continu-

ous ‘‘Fourier-modes’’ description is reasonably equivalent to, and operatively easier than, the discretized schema in the MS theory. Once assumed an effective planar description, we will consider how it can be implemented in the exact multimodal description of the fluctuation dynamics.

In a pioneering theoretical work, Zilman and Granek [35, 36] described the dynamic structure factor of fluctuating rigid membranes and provided a reliable explanation for the apparent inconsistencies that result from incomplete approaches to the MS equations (cf. the single-mode approach in eq. (9)). Strictly speaking, dynamic scattering methods, NSE among them, give access to the intermediate scattering function  $S(t)$  which contains the relevant information about the fluctuation structure factor. The scattering from a fluctuating object contains the dynamic information on the correlations between different points. Consequently, the bending contribution  $S_B(t)$  actually corresponds to a convolution between the different scatters in a deformable membrane undergoing shape fluctuations [18]. In the ZG theory, this is assumed as correlated differences in the relative positions of different points in the membrane, thus the calculation of the dynamic structure factor implies an ensemble average over the different scatters in the membrane, so that  $S_B(q, t) = S_0 \langle \exp[iq \Delta h(t)] \rangle$ , with a normalized amplitude decreasing as  $S_0 \sim q^{-2}$  [23, 37]. Because thermal fluctuations obey Gaussian statistics, by a general theorem of stochastic processes [38], such a convolution can be calculated as a Gaussian distribution of the averaged fluctuations, that is  $\langle \exp(iq \Delta h(t)) \rangle = \exp(-q^2 \langle \Delta h^2(t) \rangle / 2)$ . In rigid membranes, the shape fluctuations follow a sub-diffusive dynamics slower than the free-diffusion trajectories expected in a very soft membrane [37]. Specifically, ZG found  $\langle \Delta h^2(t) \rangle \approx (Dt)^{2/3}$  with an effective diffusion coefficient  $D \approx 0.025(k_B T / \kappa)^{1/2}(k_B T / \eta)q$  [37]; thus, for membrane phases, the fluctuating contribution to the intermediate scattering function is expected to vary as [23, 35]

$$S_B^{(\text{ZG})}(q, t) \approx \exp \left[ -(\Gamma_{\text{ZG}} t)^{2/3} \right], \quad (10)$$

with a decay rate [23, 35]

$$\Gamma_{\text{ZG}} \approx 0.025 \left( \frac{k_B T}{\kappa} \right)^{1/2} \left( \frac{k_B T}{\eta} \right) q^3. \quad (11)$$

The ZG theory predicts a stretched exponential profile for the dynamic structure factor of the fluctuating membrane. The stretched decay in eq. (10) indicates summed correlations over different modes, differently from the uncorrelated fluctuations in extremely floppy membranes, which can be approximately described by a single-exponential decay (see eq. (9)). The decay rates are expected to decrease as  $\Gamma_{\text{ZG}} \sim \kappa^{-1/2}$ , differently from the relaxation rates of the individual modes which increase with increasing bending stiffness,  $\omega_B \sim \kappa$ .

The ZG theory has been verified in dynamic light scattering [12, 39] and in NSE experiments performed at relatively low  $q$ 's [11, 40–42]. However, to fit NSE data in the ultrahigh- $q$  regime (corresponding to short distances,

**Table 1.** Chemical characteristics and relevant physical properties of the lipids used in this work.

Lipid (full name)	(Abbreviation)	Chemical purity	$T_m$ ( $^{\circ}\text{C}$ )	Lyotropic phase (at 25 $^{\circ}\text{C}$ )
1-palmitoyl-2-oleoyl- <i>sn</i> -glycero-3-phosphocholine	POPC	> 99%	-2	disordered fluid ( $l_d$ )
1,2-dimyristoyl- <i>sn</i> -glycero-3-phosphocholine	DMPC	> 99%	+23	disordered fluid ( $l_d$ )
1-stearoyl-2-myristoyl- <i>sn</i> -glycero-3-phosphocholine	SMPC	> 99%	+30	gel

of the order of the bilayer thickness,  $qh \geq 1$ ), various groups [25, 27, 43] have found it necessary to assume an apparent solvent viscosity over three times the true value. Recently, Watson and Brown [44,45] and Arriaga *et al.* [46] have argued that this discrepancy between theory and experiment can be resolved by considering dissipative mechanisms within the lipid bilayer itself. An adequate mesoscopic model of a bilayer might include not only bending motions of the bilayer as a whole but also local fluctuations in the monolayer densities. High- $k$  membrane undulations are indeed strongly affected by dilatational stresses caused by local unbalances of the monolayer densities due to curvature [13]. The importance of this hybrid mode of curvature motion coupling transverse bending with longitudinal dilation was seminaly highlighted by Evans and Yeung [13]. The dynamic theory was later developed by Seifert and Langer [47,48] on the assumption that energy dissipation within transverse bending fluctuations is controlled by bulk friction, whereas they are surface viscosities, mainly intermonolayer friction, the principal actors in the dissipation mechanism of the hybrid compression-curvature modes. Because the hybrid mode is a diffusive mode driven by the compression elasticity of the monolayers, its relaxation rate is expected to vary as  $\omega_H \approx (K/8b)k^2$  (with  $K$  being the compression modulus of the monolayers and  $b$  an intermonolayer friction coefficient) [47,48]. Bilayer dynamics within the bimodal model remains overdamped, with two coexisting modes respectively driven by bending and compression elasticity. The existence of hybrid modes was early suggested by Méléard *et al.* [49] from the dynamical analysis of the shape fluctuations of giant bilayer vesicles. In a previous work, hybrid modes were unequivocally detected in giant vesicles made of fluid lipid bilayers with different compositions [50]. The hybrid modes were proved to be an important class of curvature motion becoming progressively important with increasingly higher curvatures, whose dissipation is not governed by bulk friction, rather by intrinsic membrane viscosities [47–50]. The possible influence of this dissipation mechanism within the bilayer has previously been discussed in the context of NSE experiments [46]. However, precise expressions for the dynamic structure factor corresponding to hybrid modes are not still available thus making rigorous comparison with experiments difficult. The dominant role of an extra dissipative mode at high  $q$ 's, compatible with the hybrid mode, was proven in recent NSE experiments performed with POPC/cholesterol mixtures [46]. In that work, intermonolayer friction was tuned by adding cholesterol, a small molecule able to enhance structural coupling between monolayers through

flip-flop transport. In that regime ( $qh \geq 1$ ), very high curvatures are involved, with wavelengths shorter than membrane thickness, thus the system prefers to relax stress by exchanging cholesterol between the monolayers. Consequently, coupling between bending and dilatational motions becomes optimal at high curvatures, thus expecting the hybrid mode to dominate in this regime [39]. Alternatively, fluctuations in the membrane thickness have been hypothesized to play an important role in the same high- $q$  regime ( $qh \approx 1$ ) [51]. In this case, an excess in dynamics at the membrane thickness length scale must originate from thickness fluctuations [51].

Here, we are just concerned with a reliable method to unfold the contribution from pure-bending fluctuations to the raw NSE data obtained from different classes of undulating membranes. In this paper, we focus in the low- $q$  border of the NSE window ( $0.18 \leq q/\text{nm}^{-1} \leq 0.33$ ), at wave vectors where bending modes can be treated within the flat membrane approximation ( $qR \gg 1$ ) but hybrid modes and thickness fluctuations are still not dominating ( $qh < 1$ ). At higher  $q$ 's, those other contributions arising from the internal structure of the membrane could eventually trouble data analysis in bilayer systems. However, to give precise account of such internal modes in NSE signals, a theory of their dynamic structure factor is still lacking. In awaiting for that such theory, empiric comparisons between bilayer and non-bilayer systems with a comparable bending stiffness should help to enlighten about the optimal analytic strategies to obtain the mechanical parameters from NSE data considered over the whole  $q$ -range.

## 3 Materials and methods

### 3.1 Chemicals

Deuterated water from Sigma (99.9%) was used in all experiments as a dispersion solvent. Lipids were obtained as powders from Avanti Polar Lipids (Alabaster, AL). Their complete chemical names and relevant properties are listed in table 1.

The lipids were stored at  $-20^{\circ}\text{C}$  and used as received, without further purification. The diblock copolymer poly(butadiene-co-ethyleneoxide) (PEO<sub>29</sub>-PBD<sub>46</sub> triblock copolymer;  $M_w = 3800$  g/mol) was obtained from Polymer Source (Canada) with a minimal polydispersity ( $M_w/M_n < 1.05$ ). Pluronic L121 (PEO<sub>5</sub>-PPO<sub>68</sub>-PPO<sub>5</sub> copolymer,  $M_w = 4,400$  g/mol) was from Sigma-Aldrich. Ethanol, chloroform and other solvents were from Sigma-Aldrich.

### 3.2 Large Unilamellar Vesicles (LUVs)

LUVs were prepared by the extrusion method using a commercial minitextruder (Liposofast, AVESTIN, Canada). To avoid possible differences between DLS and NSE experiments, we always used D<sub>2</sub>O as the aqueous solvent (Sigma; 99.9%,  $\eta = 1.2010$  cPoise at 22 °C). To prepare vesicles, the powder lipid is first dissolved in a chloroform/methanol mixture (2:1). Later, the solvent is slowly removed by evaporation in a dry nitrogen stream, yielding a homogenous lipid film consisting of multiple lamellae. The lipid film is then hydrated by pouring the aqueous phase. During the hydration phase (1 h), the dispersion is frequently vortexed and maintained above the melting temperature of the lipid mixture (+10 °C; see data in table 1). Then, this lipid suspension is extruded through a polycarbonate filtering membrane (Whatman, Florham Park, NJ) with a defined pore size (200 nm), producing unilamellar vesicles with a diameter near the pore size. Extrusion is performed at a temperature well above  $T_m$ , inside an oven with the temperature fixed at  $T_m + 10$  °C. Ten extrusion cycles ensure a homogeneous dispersion of LUVs with a constant size and low polydispersity [52]. The dispersion was then filtered through a 0.2 mm teflon filter and poured into quartz tubes. The concentration of the vesicle suspensions was fixed constant at 2 mg/mL (final concentration), a value diluted enough to avoid for interaction effects. For further details on the procedures, see ref. [10].

### 3.3 CryoTEM

The sample is vitrified by the method described in refs. [53, 54]. Briefly, a few microlitres of diluted vesicle suspension (1 mg/mL *wt%*) is placed on a bare copper TEM grid (Plano, 600 mesh). The sample is cryo-fixed by rapidly immersing into liquid ethane at its freezing point. The vitrified specimen is loaded into a cryotransfer holder (CT3500, Gatan, Munich, Germany) and transferred to a Zeiss EM922 EF-TEM (Zeiss NTS GmbH, Oberkochen, Germany).

### 3.4 Dynamic Light Scattering (DLS)

DLS measurements were carried out in the ILL Soft Matter Partnership Lab (PSCM@ILL). Measurements have been performed using an ALV CGS-3 DLS/SLS Laser Light Scattering Goniometer System (ALV GmbH Langen, Germany). This instrument allows for a simultaneous measurement of static and dynamic light scattering in an angular range from 25° up to 155°. It is equipped with a HeNe laser operating at a wavelength of 633 nm with a power of 22 mW. An ALV/LSE-5004 Light Scattering Electronics is used together with a ALV-7004 Fast Multiple Tau Digital Correlator. Scattering intensities are recorded via a Pseudo-Cross Correlation setup, consisting of a fibre-optical detection unit with a fibre based

beam splitter and 2 APD detectors. For DLS measurements, a small aliquot of the same vesicle suspension prepared for NSE experiments is diluted in D<sub>2</sub>O (1:10 *v/v*). DLS (0.2 mg/mL) and NSE (2 mg/mL) experiments were indeed performed with the same vesicle suspension, DLS running immediately before NSE beamtime. The samples are poured into quartz cells (10 mm O.D., Hellma). Then, they were placed in the measurement cell which is filled with decaline to match the refractive index of the quartz sample cells. Temperature inside this cell is measured by a Pt-100 sensor and kept constant at 25.0 °C with a precision of  $\pm 0.1$  degrees. The intensity correlation function  $g^{(2)}(q, t)$  is measured using the ALV-7004 hardware correlator. This function is related to the field autocorrelation function  $g^{(1)}(q, t)$  through Siegert's relation

$$g^{(2)}(q, t) = 1 + C \left| g^{(1)}(q, t) \right|^2. \quad (12)$$

The field autocorrelation function is analyzed by CONTIN [55, 56], an algorithm based on the inverse Laplace transform. Identical results are obtained by REPES [57]. No assumption about either the number of relaxation processes or the distribution shape is required in these methods. The autocorrelation functions  $g^{(1)}(q, t)$  are described as a distribution of correlation times  $P(\Gamma)$  centred at a given relaxation rate  $\Gamma_T(q)$  and with bandwidth  $\Delta\Gamma_T$  which is an accurate estimator of the standard deviation of the relaxation rates due to sample polydispersity. No shape fluctuations exist at wave vectors smaller than the vesicle size,  $qR < 1$ . Thus, in this regime, the diffusive frequencies obtained by CONTIN must correspond to pure translational motion,  $\Gamma_T(q) = D_T q^2$ . Consequently, the hydrodynamic size of the suspended vesicles can be easily obtained by fitting the translational relaxation frequencies extracted from the DLS data to eqs. (5)-(6) in the low- $q$  limit. Within this approach, the distribution bandwidths are related with the size polydispersity as  $\sigma_R = \Delta R/R = \Delta\Gamma_T/\Gamma_T$ . Indeed, DLS is classically used to characterize the vesicles with respect to their size and polydispersity, but no internal motions can be detected in the  $qR < \pi$  regime accessible to He-Ne DLS. However, extending the DLS  $q$ -range by using UV laser lines, Cantú and co-workers were the first in revealing a fast contribution due to shape fluctuations superposed to the usual translational component [58, 59]. Those works considered an unconventional configuration with an UV source (364 nm), optimized to extend the accessible  $q$ -range to higher values, closer to the minimum of the static form factor of LUVs. The secondary relaxation detected in those works was attributed to global shape deformations of the vesicles, whose relaxation dynamics has been interpreted in terms of MS- [58, 59] and ZG models [12].

### 3.5 Neutron Spin Echo (NSE)

The reported NSE experiments were performed on the IN15 instrument at the ILL, Grenoble [60]. This instrument provides the longest Fourier times currently available

worldwide at NSE instruments. The samples are poured into quartz cells (1 mm thickness, Hellma). The instrument was equipped with a thermostatic holder for these cells and all measurements were done at a temperature of  $25.0 \pm 0.1$  °C. A Fourier time ranging up to 207 ns was explored at different  $q$ -values in the range from  $0.184 \text{ nm}^{-1}$  up to  $1.201 \text{ nm}^{-1}$ . To achieve this, measurements at a wavelength of  $\lambda = 12 \text{ \AA}$  and  $15 \text{ \AA}$  had to be performed. The wavelength distribution in both cases had a HWHM of  $\Delta\lambda/\lambda = 0.15$ .

### 3.6 NSE intermediate scattering function: Fitting procedure

In view of the theory described in sect. 2, satisfactory analysis of NSE data is only possible by unfolding translational vesicle motion and bending fluctuations through an adequate account of the relative amplitudes and proper choice of the intermediate scattering function describing the relaxation decay. Regarding the relative amplitudes, in typical lipid vesicles, translation is clearly dominant over fluctuation modes in the range of wave vectors  $qR < 20$  (see fig. 1B), a regime where translation cannot be neglected. At higher rigidities, this dominance is significantly enhanced, so the influence of the translational mode still extends up to higher  $q$ 's. For typical LUVs ( $\kappa \approx 20k_B T$ ) with a size  $R \approx 100 \text{ nm}$ , the contribution of translation to the NSE signal should be not neglected up to wave vectors  $q \gg 0.5 \text{ nm}^{-1}$  ( $qR \gg 50$ ; see fig. 1B), thus being relevant along the whole range of wave vectors accessible to NSE. Considering the ZG framework, the normalized NSE profiles might be fitted by the following expression:

$$S(t) = \exp(-D_T q^2 t) \left\{ A + (1 - A) \exp \left[ -(\Gamma_{ZG} t)^{2/3} \right] \right\}. \quad (13)$$

Because translation motion dominates over bending fluctuations, the structure factor is difficult to unfold when the  $qR < 10$  regime is scrutinized [25, 28, 61]. In this regime, it is usually approximated by an ‘‘apparent’’ bimodal function [11, 12, 59]

$$S(q, t) \approx A \exp(-D_T q^2 t) + (1 - A) \exp \left[ -(\Gamma t)^{2/3} \right], \quad (14)$$

which is valid if  $\Gamma \gg D_T q^2$ , a condition usually fulfilled in the NSE range.

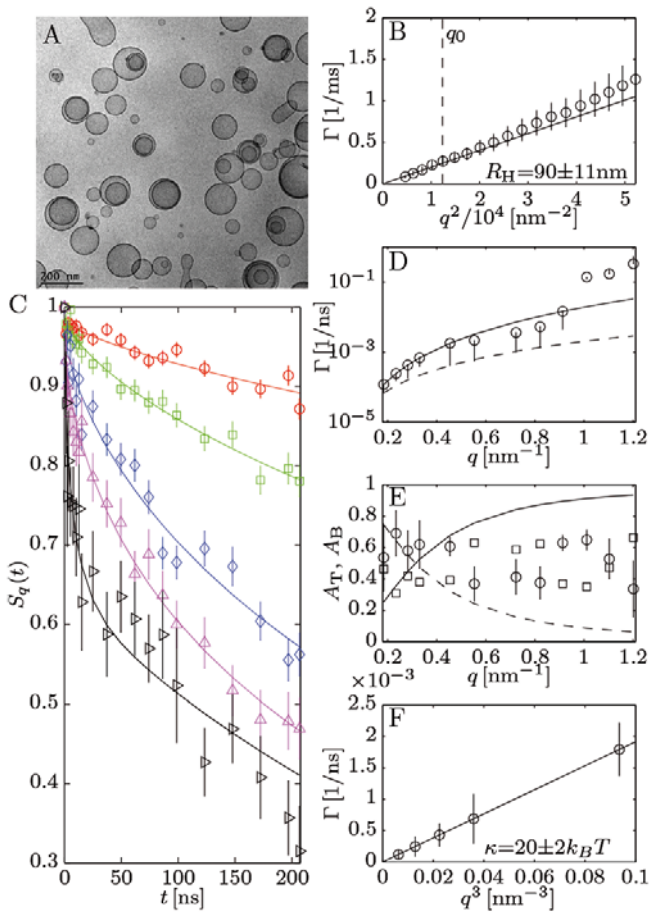
## 4 Results and discussion

In this work we study the fluctuation dynamics of vesicles made of different lipids and amphiphilic polymers. In the case of lipid bilayers, we studied vesicles made of three different phosphocholines with increasing melting temperature, POPC ( $T_m = -2$  °C), DMPC ( $T_m = 23$  °C) and SMPC ( $T_m = 30$  °C). Since higher  $T_m$  indicates increasing molecular cohesion, the bilayers of these three phospholipids must become progressively stiffer [62]. At the experimental temperature,  $T_{\text{exp}} = 25$  °C, DMPC and POPC

form fluid bilayers, however, SMPC bilayers are in the gel, solid-like, phase. In the following, the different systems are discussed separately.

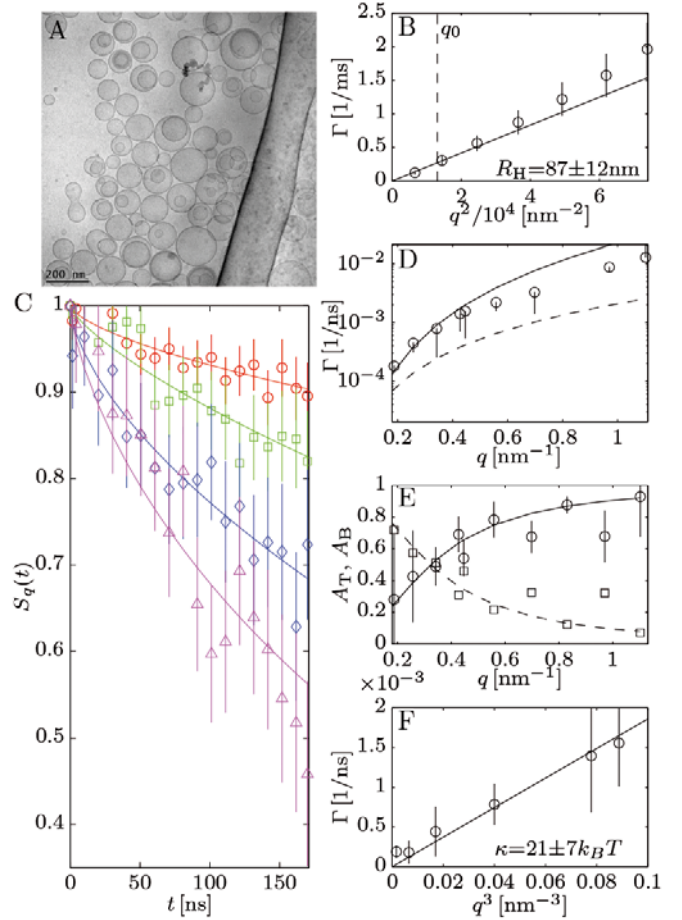
### 4.1 Fluid bilayers: DMPC and POPC

Figure 2A shows a typical cryo-TEM image of the vesicle suspensions of DMPC prepared by extrusion. Although the samples appear to be quite polydisperse ( $\pm 15\%$ , stand. dev.), most vesicles are found unilamellar and spherical, with an average size compatible with the pore size used in extrusion (200 nm, nominal diameter). A residual population of smaller vesicle objects is systematically found in all the preparations. The DLS results are displayed in fig. 2B which shows the  $q$ -dependence of the translational relaxation frequencies as obtained by CONTIN. A limiting diffusional dependence  $\Gamma_T = D_T q^2$  is observed at low  $q$ 's ( $q < q_0 = 1/R \approx 0.01 \text{ nm}^{-1}$ ). The hydrodynamic dimensions of the vesicles are calculated from the translational diffusion coefficient, obtained as the limiting slope of the linearized plot in fig. 2B. Using eqs. (5)-(6), we obtained the hydrodynamic radius  $R_h = 90 \pm 11 \text{ nm}$ , in agreement with the nominal size ( $R_{\text{nom}} = 100 \text{ nm}$ ). Above this limit (at  $q \gg q_0$ ), the influence of the small vesicles ( $< R$ ) becomes evident as a positive deviation towards faster frequencies, indicating a higher diffusivity of the smaller objects. The NSE data are shown in fig. 2C. Above the melting transition ( $T = 25$  °C  $> T_m \approx 23$  °C), DMPC membranes are expected to exhibit a reduced rigidity characteristic of the fluid phase. To fit the NSE relaxation profiles (see fig. 2C), we used the ZG expression in eq. (14) with the value of  $D_T$  obtained from the DLS data. The fitted values of the relaxation frequencies of the bending fluctuation term are shown in fig. 2D as a function of the NSE wave vector. For comparison, the relaxation rates of the master translational term are also shown in this plot (dashed line in fig. 2D). The relative amplitudes obtained from the fits are shown in fig. 2E. From our analysis, they only follow qualitatively the theoretical trends expected from a bimodal fluctuation scheme. At low  $q$ 's ( $< 0.5 \text{ nm}^{-1}$ ;  $qR < 50$ ), one observes the translational component to be dominant ( $A > 0.5$ ), with relaxation frequencies relatively close to those of the shape fluctuations. This fact clearly highlights the determinant role of the translational component in NSE data, its adequate account being absolutely mandatory for correct analysis. In the present case, however, no quantitative agreement is observed between the experimental amplitudes and the MS theory (see fig. 2E), suggesting a more complicated scenario with additional modes contributing to the NSE signals, especially at high  $q$ 's. Indeed, above  $q > 0.5 \text{ nm}^{-1}$ , the presence of hybrid modes [47, 48] and/or thickness fluctuations [51] in fluid bilayer membranes (this is DMPC at  $T > T_m$ ), could be strongly influential on the NSE intermediate relaxation function. These anomalies coincide with the range where thickness fluctuations were detected with DMPC vesicles in two different NSE instruments (NG5-NSE at NIST and IN15 at ILL) [30]. The bimodal bending/translation MS prediction is quantitative only at



**Fig. 2.** A) CryoTEM image of DMPC vesicles obtained by extrusion. B) Relaxation frequencies obtained from CONTIN analysis of the DLS data. The error bars correspond to the distribution widths  $\Delta\Gamma/\Gamma$ . The positive deviation from the  $q^2$ -dependence is due to polydispersity contributions due to faster motion of the smaller objects (at  $q > q_0 = l/R$ ). The continuous line corresponds to the linear fit to the limiting translational diffusion behavior,  $\Gamma_T = D_T q^2$ . C) NSE data ( $\circ$ :  $0.282 \text{ nm}^{-1}$ ,  $\square$ :  $0.454 \text{ nm}^{-1}$ ,  $\diamond$ :  $0.723 \text{ nm}^{-1}$ ,  $\triangle$ :  $0.913 \text{ nm}^{-1}$ ,  $\triangleright$ :  $1.011 \text{ nm}^{-1}$ ) with the lines corresponding to their respective fits to eq. (15) ( $D_T$  fixed at the DLS value;  $\beta = 3/2$ ). The fitting parameters are plotted in D): relaxation frequencies of the shape fluctuations, and E): amplitudes of translation,  $A$ , and internal mode corresponding to shape fluctuations,  $1 - A$ . The lines correspond to theoretical predictions. In D) the continuous line is the ZG frequency ( $\kappa = 20 \pm 2 k_B T$ ) and the dashed line is the relaxation frequency of the translational mode extrapolated to the NSE domain ( $\Gamma_T = D_T q^2$ , as inferred from DLS data). In E) we plot prediction lines from MS theory for translation ( $T$  dashed) and bending ( $B$  continuous) amplitudes. F) ZG plot with the  $q^3$ -dependence of the relaxation frequencies of the bending contribution to the shape fluctuations.

low  $q$  ( $< 0.5 \text{ nm}^{-1}$ ; see fig. 2E), an upper cut-off which defines the range where the bending modulus can be calculated with accuracy [30]. This is just the regime where the relaxation frequencies of the fluctuation structure factor follows  $q^3$ -scaling (see fig. 2D), a clear signature of the bending-like character of the shape fluctuations. Us-



**Fig. 3.** A) CryoTEM image of POPC vesicles obtained by extrusion. B) Relaxation frequencies obtained from CONTIN analysis of the DLS data (symbols as in fig. 2). C) NSE data with the fits, which yield the relaxation frequencies D), F) and amplitudes of translation ( $\circ$ ) and bending ( $\square$ ). F) Symbols as in C)  $q = \circ$ :  $0.119 \text{ nm}^{-1}$ ,  $\square$ :  $0.558 \text{ nm}^{-1}$ ,  $\diamond$ :  $0.830 \text{ nm}^{-1}$ ,  $\triangle$ :  $0.970 \text{ nm}^{-1}$ . Prediction lines as in fig. 2.

ing these five first points ( $q < 0.5 \text{ nm}^{-1}$ ), the bending stiffness can be accurately calculated from the  $q^3$ -plot of the ZG frequencies shown in fig. 2F. From this plot, the value of  $\kappa$  is calculated from the slope of the linear fit to eq. (11), obtaining  $\kappa = 20 \pm 2$  in  $k_B T$  units. This value is in good agreement with the literature data on DMPC mechanics [16].

A similar behavior was observed for POPC vesicles. Figure 3 reproduces previous DLS/NSE data obtained by us with LUV suspensions [11, 12]. The influence of the translational mode is obvious in view of the relative amplitudes in fig. 3E. In this case, however, a systematic negative deviation of the ZG frequencies is observed at high wave vectors,  $q > 0.4 \text{ nm}^{-1}$ . Above this limit, a third contribution was considered to account for the observed decay of the NSE signal [39]. This was interpreted as the contribution of hybrid modes to the fluctuation dynamics [39]. Indeed, at experimental conditions ( $T = 25^\circ \text{C}$ ), POPC bilayers are expected to be slightly softer under compression

and more fluid ( $K_{\text{POPC}} \approx 100 \text{ mN/m}$  [63];  $T_m = -2^\circ\text{C}$ ) than those of DMPC ( $K_{\text{DMPC}} \approx 140 \text{ mN/m}$  [64];  $T_m = 23^\circ\text{C}$ ). Furthermore, molecular disorder favors chain interdigitation in unsaturated POPC with respect to twin chains in fully saturated DMPC, promoting free-sliding between the bilayers in the later case. Consequently, lower relaxation rates are expected for the hybrid mode,  $\omega_H \approx (K/8b)k^2$ , in POPC than in DMPC bilayers. This could explain why no evident dissipative signatures of hybrid modes were detected in the NSE signals of DMPC [30] and of other saturated phospholipids like DPPC, DSPC [30], whereas clear evidence of hybrid dynamics was detected in POPC bilayers [39]. Considering only the first five points ( $q < 0.5 \text{ nm}^{-1}$ ), where bending motions are expected to be dominant over hybrid modes [46], a reasonable value of the bending stiffness  $\kappa = 21 \pm 7k_B T$  is obtained from the fit of the ZG frequencies in the  $q^3$ -plot (see fig. 3F). This value is in agreement with literature data. Indeed, the bending elasticity of POPC bilayers has been extensively studied in micropipette experiments performed on GUVs [64] and from X-ray experiments on the lamellar  $L_D$  phase [65] ( $\kappa \approx 20k_B T$ , at room temperature). Similarly to the case of DMPC, this elasticity assigns fluid membranes made of POPC with a rigid character, both, upon bending ( $\kappa \approx 20k_B T$ ) and compression ( $K \approx 100\text{--}140 \text{ mN/m}$ ) [16, 63, 64].

#### 4.2 Rigid solid-like bilayers: SMPC

The case of SMPC is particularly interesting. A solid-like character is expected below its melting temperature ( $T_m = 30^\circ\text{C}$ ), forming gel bilayers at the experimental conditions ( $T = 25^\circ\text{C}$ ). The marked dissymmetry of the two saturated chains (C18:0 stearoyl, myristoyl C14:0 PC) favors a high chain interdigitation between the monolayers. Consequently, at experimental conditions SMPC vesicles are expected to behave as solid shells able to undergo weak shape fluctuations by contrast to floppy vesicles with a fluid membrane (case of DMPC and POPC in sect. 4.1). The cryo-TEM images in fig. 4A clearly reveal the solid character of SMPC vesicles. The presence of flat edges indicates high membrane rigidity (see high-resolution inset in fig. 4A), characteristic of solid-like membranes. A pure diffusive behavior is observed in the DLS relaxation rates (see fig. 4B), the data being perfectly described just by a translational scaling over the whole range of studied wave vectors. We plot in fig. 4C the NSE signals, which are observed to decay significantly, at levels even lower than observed in fluid POPC vesicles (see fig. 3C). Since extremely weak shape fluctuations are expected in a solid membrane, undoubtedly, it is the translation component that mainly contributes to these decaying signals. This is clearly demonstrated by figs. 4D and E, where the dynamical parameters are plotted as obtained from the fits to the translation/bending structure factor (eq. (13)). The ZG frequencies are found slower than for DMPC and POPC, as expected for a more rigid membrane ( $\Gamma_{\text{ZG}} \sim \kappa^{-1/2}$ ). A higher rigidity causes indeed the characteristic frequencies of the shape fluctuations to merge with the transla-

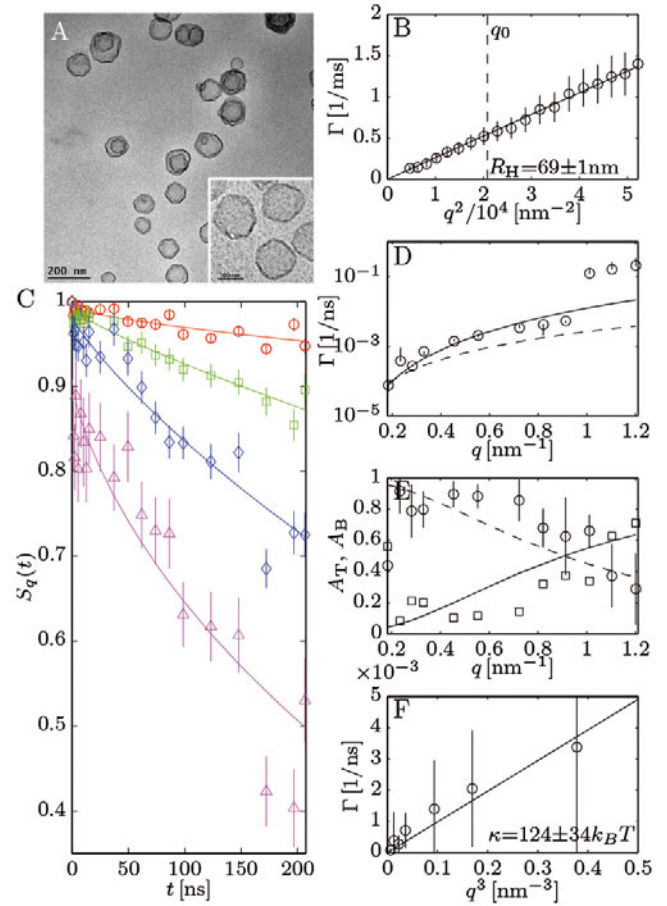


**Fig. 4.** A) CryoTEM image of SMPC vesicles obtained by extrusion. The straight borders along the vesicles contours indicate that they were in the gel state at room temperature before being vitrified. In the magnified inset the bilayer structure of the membrane is visible. B) Relaxation frequencies obtained from CONTIN analysis of the DLS data. The absence of the  $q^2$ -dependence observed in the other datasets is indicative of the gel-state of vesicle membranes during measurement. C) NSE data with the fits, which yield the relaxation frequencies D), F) and amplitudes of translation ( $\circ$ ) and bending ( $\square$ ) F). Symbols in C)  $q = \circ$ :  $0.184 \text{ nm}^{-1}$ ,  $\square$ :  $0.454 \text{ nm}^{-1}$ ,  $\diamond$ :  $0.723 \text{ nm}^{-1}$ ,  $\triangle$ :  $0.913 \text{ nm}^{-1}$ . Prediction lines as in fig. 2.

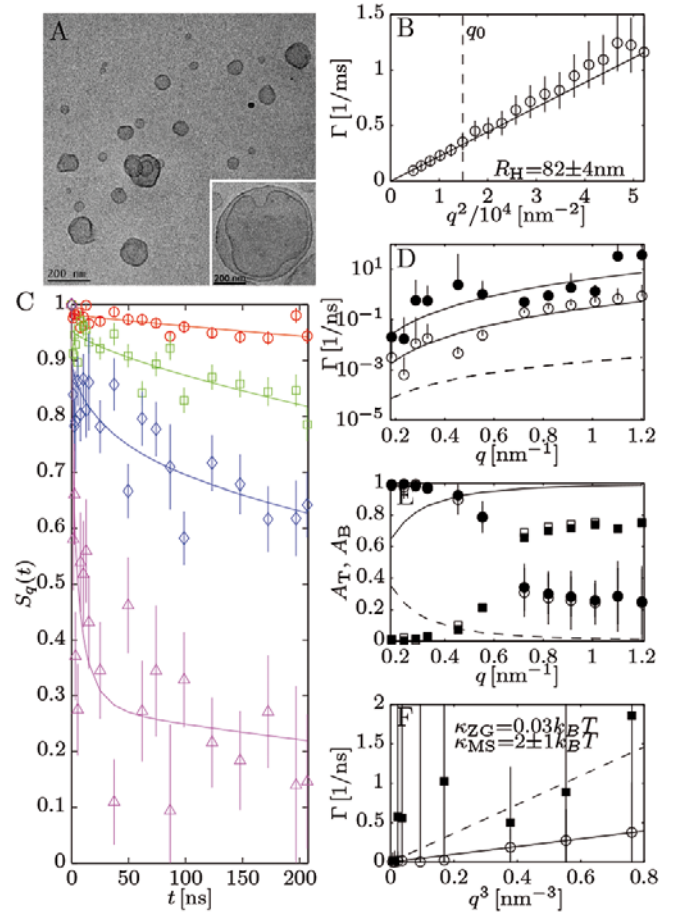
tional frequencies ( $\Gamma_{\text{ZG}} \rightarrow \Gamma_T$ ; see fig. 4D). The bimodal model is still able to split the two components, the translational one being clearly dominant except for the highest wave vectors (see fig. 4E). In this case, a value of  $\kappa$  can be still calculated from the ZG fluctuation frequencies. A value  $\kappa = 124 \pm 34k_B T$  is obtained from the  $q^3$ -plot in fig. 4E. Similar high rigidities have been recently reported from NSE experiments performed with other fully saturated phospholipids below the melting transition [30]. In the present case, NSE measurements were performed at  $25^\circ\text{C}$ , only  $-5^\circ\text{C}$  below the melting transition of the phospholipid ( $T_m = 30^\circ\text{C}$ ). Upon solidification, the bending modulus of lipid bilayers is assumed to increase drastically between a low value corresponding to the high-temperature fluid phase ( $10\text{--}20k_B T$ , typically) up to a

much higher value in the gel/solid state, well below  $T_m$ . However, such a structural stiffening is observed to occur in a broad temperature interval below  $T_m$ , where  $\kappa$  increases smoothly [16]. For instance, in DPPC bilayers ( $T_m = 41^\circ\text{C}$ ), the transition region is so broad as  $-5^\circ\text{C}$  below  $T_m$ , as observed by NSE experiments [66, 67]. The value reported here for SMPC at  $25^\circ\text{C}$  ( $\kappa = 124k_B T$ ,  $-5^\circ\text{C}$  below  $T_m$ ), probably represents an intermediate state in the transition region, mechanically softer than the rigid solid at a temperature well below  $T_m$ . No trace of hybrid modes is detected in these solid-like systems, where the high coupling between the monolayers prevents from relative slippage and thus the coupling of transverse movements to longitudinal motions.

### 4.3 Polymer membranes: soft L121 vs. rigid rubber

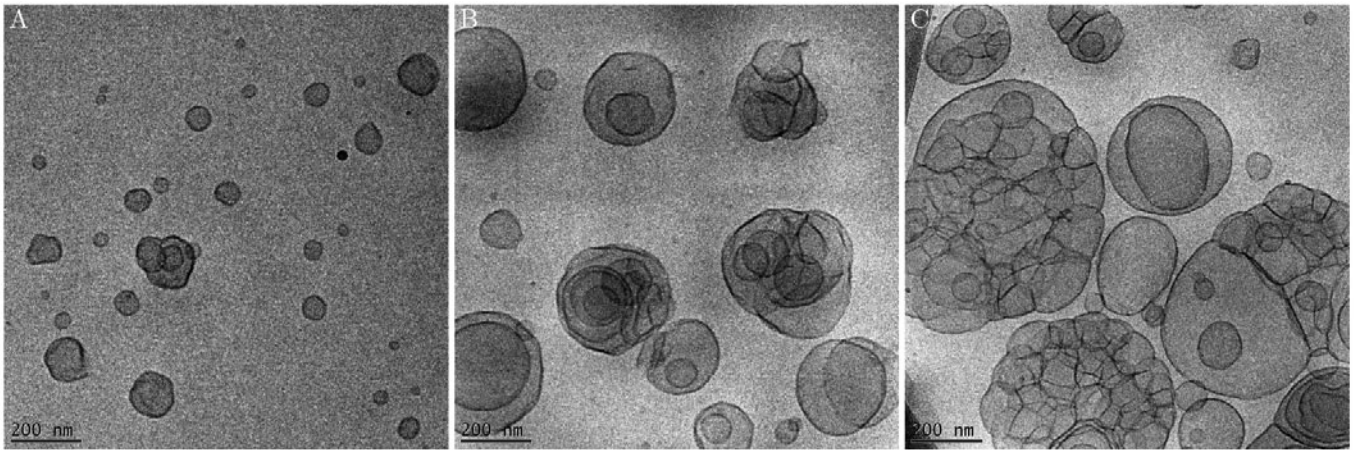
Aiming at an understanding of compact structureless membranes, we measured NSE intermediate scattering functions from diluted polymersome dispersions. Two amphiphilic polymer systems, able to form vesicles, were considered: the triblock copolymer Pluronic L121 and the diblock rubber PBD-PEO. The soluble Pluronic L121 is formed by a central, slightly hydrophobic, block of polypropylenoxide (PPO) flanked by two small lateral chains of the hydrophilic polyethylenoxide (PEO). The rubbery copolymer, PBD-PEO is formed by a very hydrophobic block of polybutadiene (PBD) linked to a highly flexible coil of soluble PEO. These two copolymers are known to form stable vesicles (polymersomes) with extreme rigidities and very different permeability to water [68]. On one hand, L121 assembles as a floppy membrane with a relatively low degree of chain entanglement inside the hydrophobic core, thus being highly permeable to water. On the other hand, PBD-PEO assembles into a rubbery hydrophobic core which endows the system with a frozen-like structure highly impermeable to water. In both cases, relative motions between the two leaflets are strongly hindered by a high degree of macromolecular entangling thus behaving as a compact layer. These systems were chosen to span a broad range of membrane stiffness with a different molecular architecture; whilst phospholipids can form soft or rigid bilayers with more or less degree of sliding between the monolayers, block copolymers self-assemble with a compact sheet structure with these two leaflets fused together.

Figure 5A shows a cryo-TEM image of a diluted suspension of L121 polymersomes. One finds highly deformable structures typical of very soft membranes (see high-resolution inset in fig. 5A) with a high degree of aggregation promoted by surface adhesion (see fig. 6). The NSE signals show in this case significant relaxation (fig. 5C). Data analysis using the bimodal model with the ZG expression (eq. (13)) provides very high frequencies for the shape fluctuations well separated from the translational component (see fig. 5D). The ZG frequencies follow  $q^3$ -scaling (see fig. 5E), as expected for membranes whose elasticity is exclusively governed by pure-bending motions. The analysis of the relaxation frequencies with eq. (13)



**Fig. 5.** A) CryoTEM image of vesicles formed from the triblock polymer L121 by extrusion. The inset shows the magnification of a floppy vesicle exemplifying the low bending rigidity of L121 membranes. B) Relaxation frequencies obtained from CONTIN analysis of the DLS data. The positive deviation from the  $q^2$ -dependence is due to contributions of the bending mode as we cross  $q_0$ . C) NSE data with the fits, which yield the relaxation frequencies D), F) and amplitudes of translation ( $\circ$ ) and bending ( $\square$ ) F). Symbols in C)  $q = \circ$ :  $0.282 \text{ nm}^{-1}$ ,  $\square$ :  $0.454 \text{ nm}^{-1}$ ,  $\diamond$ :  $0.553 \text{ nm}^{-1}$ ,  $\triangle$ :  $0.723 \text{ nm}^{-1}$ . Prediction lines as in fig. 2. Doubled symbols in D)-F) correspond to parameters obtained with different fits: ZG ( $\beta = 2/3$ ; open symbols), MS ( $\beta = 1$ ; closed symbols).

provides a very low value  $\kappa = 0.03k_B T$ , corresponding to extremely soft-membrane behavior. Hence, the NSE data were re-analyzed using the bimodal model with a single-exponential profile for the fluctuation form factor (eq. (9)). From the fits, new relaxation frequencies were obtained in rough agreement with the ZG values (see fig. 5D). In this case, the analysis of the  $q^3$ -plot with eq. (3) provided a value  $\kappa = 2 \pm 1k_B T$ , which is more reasonable and in agreement with previous dynamical experiments using flickering spectroscopy with giant vesicles [68, 69]. The relative amplitudes in fig. 5E are found consistent between the two methods. However, a dominance of the translational component, higher than theoretically expected, is revealed from the experimental values. This could be related to the



**Fig. 6.** Series of CryoTEM images of samples taken from the same L121 preparation and vitrified at increasing times after extrusion (A) immediately after; B) after 1 h; C) after 4 h). As time progresses the vesicles become increasingly agglomerated and fuse together to form ever larger vesicles in the aggregates.

high polydispersity of sizes and shapes characteristics of these polymersome samples. Figure 6 shows a gallery of images of the same L121 sample which was subjected to cryo-fixation at progressive longer times. The presence of large aggregates of adhered polymersomes is evident with time, which could explain a progressive dominance of the translational component.

The results for the rigid PBD-PEO copolymer are shown in fig. 7. The cryo-TEM images in fig. 7A reveal the existence of rubbery membranes, thicker and denser than those found for L121 [68, 69]. In this case, no vesicle adhesion is observed in the microscopy images. Deviations with respect to the diffusional translation limit are observed in the DLS frequencies (see fig. 7B), which suggest a relevant contribution from the shape fluctuation modes. This influence is evident after the analysis of the NSE relaxation curves in fig. 7C. The bimodal translation/bending model reveals two separated components with amplitudes compatible with theory (see fig. 7E). At low  $q$ 's, the ZG frequencies are found close to the translational component but compatible with  $q^3$ -scaling (see fig. 7D). However, a sudden rise up to a much faster regime is detected at  $q > q_h \approx 0.5 \text{ nm}^{-1}$ . For the calculation of the bending modulus only the first five points below  $q_h$  were considered within the ZG equation (eq. (11)). A value  $\kappa = 46 \pm 22 k_B T$  was obtained from the  $q^3$ -plot in fig. 7F, in agreement with literature data obtained for giant polymersomes of this polymer using flickering spectroscopy [69] and micropipette aspiration [70]. The deviation that we observe in fig. 7D corresponds to a very localized excursion at a wavelength around  $\lambda = 2\pi/q_h \approx 12 \text{ nm}$ , compatible with the membrane thickness [39], which registers as an enhancement rather than a suppression of the  $q^3$ -dependence. A similar excess in dynamics at the membrane thickness length scale has been interpreted by Nagao and collaborators [30, 71, 72] as the signature of the transversal fluctuations in membrane thickness. Such a kind of peristaltic pumping is expected to drive a shift in

the frequencies of the bending mode as

$$\Gamma_B^{(h)} = \Gamma_B + \left(\frac{q}{q_h}\right)^3 \frac{\Gamma_{\text{per}}}{1 + (q - q_0)^2 \xi^{-2}}, \quad (15)$$

where  $\Gamma_B^{(h)}$  indicates the renormalized decay rate of the bending fluctuations and  $\Gamma_{\text{per}}$  represents the decay rate due to the thickness fluctuations, leading to the excess dynamics observed at  $q_h$ .  $\xi$  is a characteristic distance of the order of the amplitude of the thickness fluctuation. Thickness fluctuations should be controlled by geometrical constraints, such as volume conservation. Similarly to the thickness fluctuations found in surfactant membranes [71], the average amplitude was estimated to be  $\xi \approx 1 \text{ nm}$ , approximately 10% of the membrane thickness. A prediction for  $q_h = 0.5 \text{ nm}^{-1}$ ,  $\Gamma_{\text{per}} = 2 \cdot 10^7 \text{ s}^{-1}$  and  $\xi = 1 \text{ nm}$  is plotted in fig. 7D, in close agreement with experimental observation. The computed relaxation time of the thickness fluctuation,  $\tau = 1/\Gamma_{\text{per}}$ , is on the order of 50 ns, longer than the few nanoseconds estimated in surfactant membranes [25, 72], but compatible with the idea of a entangled hydrophobic core with a slow relaxation of the rubbery internal modes.

## 5 Conclusions

From the NSE data reported here, the presence of shape fluctuations concomitant with a master translational component has been clearly evidenced in diluted suspensions of unilamellar vesicles made of different lipids and amphiphiles. The two components can be unfolded from the intermediate scattering function using a bimodal exponential decay (eq. (14)) with a fluctuation term as a stretched exponential. This is compatible with the Zilman-Granek theory which provides the adequate theoretical frame for describing the relaxation rate of the shape fluctuations of rigid membranes which are driven by a combination

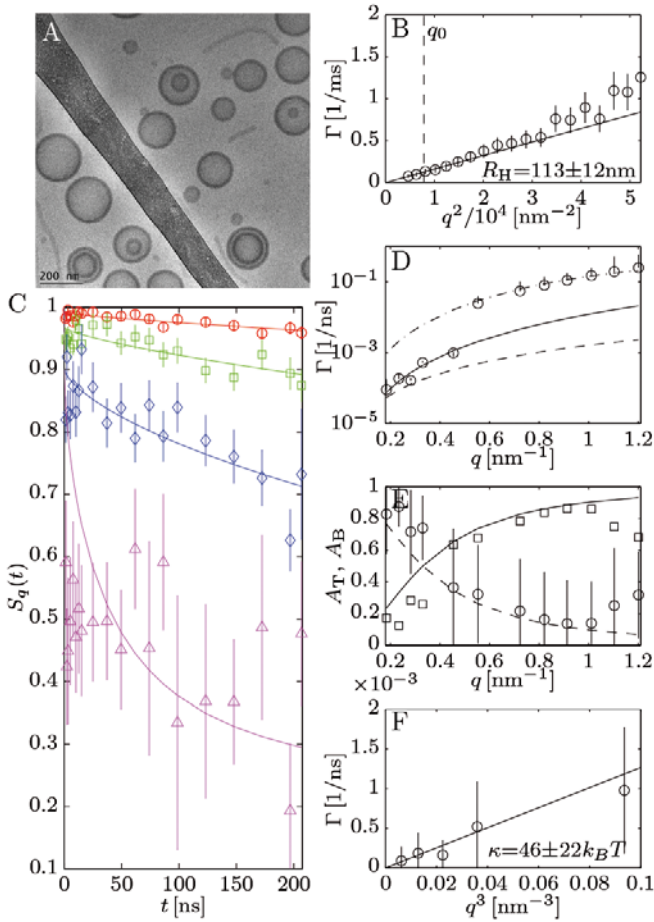


**Fig. 7.** A) CryoTEM image of vesicles formed from the rubbery polymer PBD-PED by extrusion. B) Relaxation frequencies obtained from CONTIN analysis of the DLS data. The positive deviation from the  $q^2$ -dependence is due to contributions of the shape fluctuations as we cross  $q_0$ . C) NSE data with the fits, which yield the relaxation frequencies D), F) and amplitudes of translation ( $\circ$ ) and bending ( $\square$ ) F). Symbols in C)  $q = \circ$ :  $0.234 \text{ nm}^{-1}$ ,  $\square$ :  $0.330 \text{ nm}^{-1}$ ,  $\diamond$ :  $0.454 \text{ nm}^{-1}$ ,  $\triangle$ :  $0.553 \text{ nm}^{-1}$ . Predictions lines as in fig. 2. The dash-dotted line in D) corresponds to the dynamic increase predicted from thickness fluctuations (see eq. (15) and discussion therein).

of pure-bending modes. The fluctuation component, scaling as  $\sim q^3$ , is found usually faster than the translational one which varies as  $\sim q^2$ . This dynamic separation enables adequate unfolding of the two components through classical minimization methods. The higher the bending rigidity, the slower the relaxation rate of the bending component ( $\Gamma_{ZG} \sim \kappa^{-1/2}$ ) which could eventually collapse within the translational process. In these cases, precise knowledge of the relative amplitudes of the two components should be determinant for accurate determination of the bending modulus from the ZG frequencies. From the ZG analysis, which is essentially equivalent to the complete MS description, values of the bending stiffness can be obtained using the adequate range of experimental wave vectors where additional modes of curvature motion do not have a relevant role yet. Shape fluctuations in vesi-

cles with a low rigidity ( $\kappa \approx k_B T$ ), however, could be treated using the single-mode scheme. Such an experimental feature, early reported from NSE experiments in soft microemulsion phases [21], is still awaiting further theoretical explanation. We can conclude therefore that the ZG theory represents the adequate formalism to probe dynamic relaxation in rigid bilayers, where curvature modes are inefficient in exploring the bulk medium for adequate dissipation. The MS theory captures all the essential dynamical features of fluctuating membranes, however, in its simplified form as a single exponential (eq. (9)) it fails to describe relaxation involved in NSE signals of rigid membranes. However, the complete MS theory, through the equivalent ZG structure factor obtained under the continuous planar modes approximation, might be the method of choice to interpret NSE signals with spherical vesicles. In either of the two cases, rigid or floppy, a proper consideration of the translational component and of possible modes of curvature motion alternative to bending fluctuations is essential for an adequate calculation of the bending modulus. However, whereas precise account of the relaxation profile of the pure-bending component is provided by the ZG theory, a similar approach for other modes of shape fluctuation is still lacking. Therefore, and trying to answer the question posed in the title of this article, we can assert that taking the appropriate considerations, NSE is adequate to assess the bending stiffness of biological membranes, although additional components of membrane mechanics could eventually contribute to shape the intermediate scattering function.

This work was funded by MICINN under grants FIS2012-35723, FIS2009-14650-C02-01, Consolider-Ingenio 2010 en “Nanociencia Molecular” (CSD2007-0010) and S2009MAT-1507 (NOBIMAT) from CAM. M. Mell was supported by FPU Program (MEC) and L.H. Moleiro by CSD2007-0010. I. López-Montero thanks support from NOBIMAT (CAM). We gratefully acknowledge ILL Soft Matter Partnership Lab (PSCM@ILL) for DLS-time in its facility. We are grateful to Markus Drechsler (Bayreuth University) for technical assistance with cryo-TEM.

## References

1. W. Helfrich, Z. Naturforsch. c **28**, 693 (1973).
2. J.F. Nagle, S. Tristram-Nagle, Biochim. Biophys. Acta **1469**, 159 (2000).
3. J. Lyatskaya, Y. Liu, S. Tristram-Nagle, J. Katsaras, J.F. Nagle, Phys. Rev. E **63**, 011907 (2000).
4. G. Brotons, L. Belloni, Th. Zemb, T. Salditt, Europhys. Lett. **75**, 992 (2006).
5. M.M. Blum, M. Mustyakimov, H. Rüterjans, K. Kehe, B.P. Schoenborn, P. Langan, J.C. Chen, Proc. Natl. Acad. Sci. U.S.A. **106**, 713 (2009).
6. E. Schneck, B. Demé, C. Gege, M. Tanaka, Biophys. J. **100**, 2151 (2011).
7. V.I. Gordeliy, M.A. Kiselev, Biophys. J. **69**, 1424 (1995).
8. J. Pencer, F.R. Hallett, Phys. Rev. E **61**, 3003 (2000).

9. P.C. Mason, B.D. Gaulin, R.M. Epand, G.D. Wignall, J.S. Lin, *Phys. Rev. E* **59**, 3361 (1999).
10. N. Kucerka, J.F. Nagle, S.E. Feller, P. Balgavý, *Phys. Rev. E* **69**, 051903 (2004).
11. L.R. Arriaga, I. López-Montero, F. Monroy, G. Orts-Gil, B. Farago, T. Hellweg, *Biophys. J.* **96**, 3629 (2009).
12. L.R. Arriaga, I. López-Montero, G. Orts-Gil, B. Farago, T. Hellweg, F. Monroy, *Phys. Rev. E* **80**, 031908 (2009).
13. E. Evans, A. Yeung, *Chem. Phys. Lipids* **73**, 39 (1994).
14. J.T. Jenkins, *J. Math. Biol.* **4**, 149 (1977).
15. M.B. Schneider, J.T. Jenkins, W.W. Webb, *J. Phys. (Paris)* **45**, 1457 (1984).
16. D.A. Boal, *Mechanics of the Cell*, 2nd edition (Cambridge University Press, Cambridge, 2012).
17. W. Helfrich, R.-M. Servuss, *Nuovo Cimento D* **3**, 137 (1984).
18. B.J. Berne, R. Pecora, *Dynamic Light Scattering* (Wiley, New York, 1976).
19. S.W. Lovesey, P. Schofield, *J. Phys. C: Solid State Phys.* **9**, 2843 (1976).
20. S.T. Milner, S.A. Safran, *Phys. Rev. A* **36**, 4371 (1987).
21. T. Hellweg, D. Langevin, *Phys. Rev. E* **57**, 6825 (1998).
22. R. Messenger, P. Bassereau, G. Porte, *J. Phys. (Paris)* **51**, 1329 (1990).
23. A.G. Zilman, R. Granek, *Chem. Phys.* **284**, 195 (2002).
24. J.S. Huang, S.T. Milner, B. Farago, D. Richter, *Phys. Rev. Lett.* **59**, 2600 (1987).
25. B. Farago, M. Monkenbusch, K.D. Goecking, D. Richter, J.S. Huang, *Physica B* **213-214**, 712 (1995).
26. T. Hellweg, A. Brûlet, T. Sottmann, *Phys. Chem. Chem. Phys.* **2**, 5168 (2000).
27. S. Komura, T. Takeda, Y. Kawabata, S.K. Ghosh, H. Seto, M. Nagao, *Phys. Rev. E* **63**, 041402 (2001).
28. B. Farago, M. Gradzielski, *J. Chem. Phys.* **114**, 10105 (2001).
29. M. Mihailescu, M. Monkenbusch, J. Allgaier, H. Frielinghaus, D. Richter, B. Jakobs, T. Sottmann, *Phys. Rev. E* **66**, 041504 (2002).
30. A.C. Woodka, P.D. Butler, L. Porcar, B. Farago, M. Nagao, *Phys. Rev. Lett.* **109**, 058102 (2012).
31. E. Freyssingeas, D. Roux, F. Nallet, *J. Phys.: Condens. Matter* **8**, 2801 (1996).
32. E. Freyssingeas, F. Nallet, D. Roux, *Langmuir* **12**, 6028 (1996).
33. J.F. Faucon, M.D. Mitov, P. Méléard, I. Bivas, P. Bothorel, *J. Phys. (Paris)* **50**, 2389 (1989).
34. J. Pécréaux, H.G. Döbereiner, J. Prost, J.-F. Joanny, P. Bassereau, *Eur. Phys. J. E* **13**, 277 (2004).
35. A.G. Zilman, R. Granek, *Phys. Rev. Lett.* **77**, 4788 (1996).
36. R. Granek, *Soft Matter* **7**, 5281 (2011).
37. R. Granek, *J. Phys. II* **7**, 1761 (1997).
38. N.G. van Kampen, *Stochastic Process in Physics and Chemistry* (North-Holland, Amsterdam, 1992).
39. R. Iñiguez-Palomares, H. Acuña-Campa, A. Maldonado, *Phys. Rev. E* **84**, 011604 (2011).
40. M.H. Nagao, H. Seto, Y. Kawabata, T. Takeda, *J. Appl. Crystallogr.* **33**, 653 (2000).
41. M. Mihailescu, M. Monkenbusch, H. Endo, J. Allgaier, G. Gompper, J. Stellbrink, D. Richter, B. Jakobs, T. Sottmann, B. Farago, *J. Chem. Phys.* **115**, 9563 (2001).
42. Z. Yi, M. Nagao, D. Bossev, *J. Phys.: Condens. Matter* **21**, 155104 (2009).
43. M. Imai, R. Mawatari, K. Nakaya, S. Komura, *Eur. Phys. J. E* **13**, 391 (2004).
44. M.C. Watson, F.L.H. Brown, *Biophys. J.* **98**, L9 (2010).
45. M.C. Watson, Y. Peng, Y. Zheng, F.L.H. Brown, *J. Chem. Phys.* **135**, 194701 (2011).
46. L.R. Arriaga, R. Rodríguez-García, I. López-Montero, B. Farago, T. Hellweg, F. Monroy, *Eur. Phys. J. E* **31**, 105 (2010).
47. U. Seifert, S.A. Langer, *Europhys. Lett.* **23**, 71 (1993).
48. M. Kraus, U. Seifert, *J. Phys. II* **4**, 1117 (1994).
49. T. Pott, P. Méléard, *Europhys. Lett.* **59**, 87 (2002).
50. R. Rodríguez-García, L.R. Arriaga, M. Mell, L.H. Moleiro, I. López-Montero, F. Monroy, *Phys. Rev. Lett.* **102**, 128201 (2009).
51. M. Nagao, *Phys. Rev. E* **80**, 031606 (2009).
52. B.J. Frisken, C. Asman, P.J. Patten, *Langmuir* **16**, 928 (2000).
53. Z. Li, E. Kesselman, Y. Talmon, M.A. Hillmyer, T.P. Lodge, *Science* **306**, 98 (2004).
54. A. Wittmann, M. Drechsler, Y. Talmon, M. Ballauff, *J. Am. Chem. Soc.* **127**, 9688 (2005).
55. S.W. Provencher, *Comput. Phys. Commun.* **27**, 213 (1982).
56. S.W. Provencher, *Comput. Phys. Commun.* **27**, 229 (1982).
57. A. Jakes, *Collect. Czech. Chem. Commun.* **60**, 1781 (1995).
58. P. Brocca, L. Cantù, M. Corti, E.D. Favero, *Prog. Colloid Polym. Sci.* **115**, 181 (2000).
59. P. Brocca, L. Cantù, M. Corti, E.D. Favero, S. Motta, *Langmuir* **20**, 2141 (2004).
60. P. Schleger *et al.*, *Physica B* **266**, 49 (1999).
61. B. Farago, D. Richter, J.S. Huang, S.A. Safran, S.T. Milner, *Phys. Rev. Lett.* **65**, 3348 (1990).
62. D. Chapman, *Q. Rev. Biophys.* **8**, 185 (1975).
63. I. López-Montero, L.R. Arriaga, G. Rivas, M. Vélez, F. Monroy, *Chem. Phys. Lipids* **163**, 56 (2010).
64. W. Rawicz, K.C. Olbrich, T. McIntosh, D. Needham, E. Evans, *Biophys. J.* **79**, 328 (2000).
65. N. Kucerka, S. Tristram-Nagle, J.F. Nagle, *J. Memb. Biol.* **208**, 193 (2005).
66. A.C. Woodka, P.D. Butler, L. Porcar, B. Farago, M. Nagao, *Phys. Rev. E* **80**, 031606 (2009).
67. H. Seto, N.L. Yamada, M. Nagao, M. Hishida, T. Takeda, *Eur. Phys. J. E* **26**, 217 (2008).
68. R. Rodríguez-García, M. Mell, I. López-Montero, J. Netzel, T. Hellweg, F. Monroy, *Soft Matter* **7**, 1532 (2011).
69. R. Rodríguez-García, M. Mell, I. López-Montero, F. Monroy, *Europhys. Lett.* **94**, 28009 (2011).
70. H. Bermúdez *et al.*, *Macromolecules* **35**, 8203 (2002).
71. M. Nagao, S. Chawang, T. Hawa, *Soft Matter* **7**, 6598 (2011).
72. M. Nagao, *J. Chem. Phys.* **135**, 074704 (2011).